# Heat transfer rate and uniformity of mist flow jet impingement for glass tempering

Pingping Yu [a], Keqian Zhu [a], Tao Sun [a], Ningyi Yuan [a,*], Jianning Ding [a,b,*]

[a] School of Mechanical Engineering, Jiangsu Collaborative Innovation Center for Photovoltaic Science and Engineering, Jiangsu Province Cultivation base for State Key Laboratory of Photovoltaic Science and Technology, Changzhou University, Changzhou 213164, China
[b] Micro/Nano Science and Technology Center, Jiangsu University, Zhenjiang 212013, China

## ABSTRACT

The thinning and miniaturization of components, such as liquid crystal display and solar cells, has increased the market demand for tempered ultra-thin glass. The physical tempering in glass, which is less than 2 mm thick, is difficult to achieve in air jet impingement. In this study, we propose the use of mist flow jet impingement cooling technology on ultra-thin glass. The effects of the mist flow droplets diameters, nozzle inlet temperature, and mass fraction on the heat transfer rate and uniformity are numerically studied. Our performance in terms of the heat transfer rate and the uniformity is accounted for through an evaluation of the surface-averaged temperature, averaged Nusselt number, surface-averaged Nusselt number, and surface standard deviation percentage of the Nusselt number. The empirical correlation for the surface averaged Nusselt number as a function of mist flow droplet diameters is provided. The droplet diameter is the major factor affecting the heat transfer rate, while the jet inlet temperature is a minor factor. We can obtain a better heat transfer uniformity by controlling the droplet diameter of the mist flow jet impingement. Using mist flow jet impingement, we would not only greatly reduce the amount of air and save energy, but also meet the needs of sudden cooling for tempered glass with a thickness of less than 2 mm.

© 2017 Published by Elsevier Ltd.

## 1. Introduction

The thinning and miniaturization of components, such as liquid crystal display and solar cells, has increased the market demand for ultra-thin glass. In these applications, the ultra-thin glass should be tempered to ensure the strength and safety of final products. During the glass tempering process, glass is heated close to its melting temperature, and then exposed to a sudden cooling process with fluid jets. This sudden cooling results in a sharp contraction of the glass surface, thereby generating compressive stress in the outer regions of the glass, while simultaneously slowing tensile stress formation in the inner regions [1].

The jet impingement heat transfer characteristics of 4–6-mm-thick glass samples are presently being investigated [2–7]. The physical tempering in glass, which is less than 2 mm thick, is difficult to achieve in air jet impingement [8]. The jet impingement

heat transfer during glass tempering is usually performed under conditions of high temperature difference and small jet-to-plate distance.

Glass tempering experiments on the water spray cooling method with different thicknesses (2.1–4.9 mm) [9–11] have also been studied. However, spray cooling can cause the uneven heat transfer [12]. The Non-uniformity of the glass surface temperature causes an uneven stress distribution in the glass, which can result in fragility.

Experimental studies [13–15] and simulations [16–20] on air-mist jet impingement heat transfer have mainly focused on other applications, with conditions being large jet-to-plate distances and a small temperature difference between the nozzle inlet and the target plate, instead of glass tempering. However, in obtaining ultra-thin tempered glass, we need not only a shorter cooling time and faster surface cooing during the glass tempering, but also a uniformity of the surface temperature, which has a large effect on glass tempering. Hence, the heat transfer rate and uniformity of the mist flow jet impingement in the glass tempering process are studied.

Most of the abovementioned studies focused on the enhancement of the heat transfer rate and the experiments on the glass

* Corresponding authors at: Jiangsu Collaborative Innovation Center for Photovoltaic Science and Engineering, Jiangsu Province Cultivation base for State Key Laboratory of Photovoltaic Science and Technology, Changzhou University, Changzhou 213164, China.
 *E-mail addresses:* nyyuan@cczu.edu.cn (N. Yuan), dingjn@cczu.edu.cn (J. Ding).

**Nomenclature**

| | |
|---|---|
| $a_1, a_2, a_3$ | constant experimental parameters |
| $B_i$ | Biot number |
| $C_D$ | drag coefficient |
| $C_p$ | specific heat capacity J/(kg K) |
| D | nozzle diameter (mm) |
| $d_p$ | droplet diameter (μm) |
| $F_x$ | additional acceleration force (N/kg) |
| h | heat transfer coefficient (W/m² k) |
| H | jet to impingement plate distance (mm) |
| $h_{fg}$ | latent heat (J/kg) |
| $\dot{m}$ | mass flow rate of the droplets (kg/s) |
| $M_{L1}$ | mass fraction of droplets |
| $N_u$ | Nusselt number |
| $N_{u_{ave}}$ | averaged Nusselt number |
| $\overline{N_u}$ | surface averaged Nusselt number |
| $P_r$ | Prandtl number |
| $q''$ | wall heat flux (W/m²) |
| $R_e$ | Reynolds number |
| $S_h$ | source term of energy (J/m³ s) |
| $S_m$ | source term of mass (kg/m³ s) |
| T | temperature (K) |

| | |
|---|---|
| ΔT | temperature difference (K) |
| u | fluid velocity (m/s) |
| x | axial distance along impingement plate (mm) |
| y | distance along impingement plate width (mm) |

*Greek symbols*

| | |
|---|---|
| $\rho$ | density (kg/m³) |
| $\lambda$ | thermal conductivity (W/K m) |
| $\mu$ | dynamic viscosity (kg/m s) |
| $\xi$ | heat transfer enhancement ratio |
| $\sigma_{N_u}$ | surface standard deviation percentage of the Nusselt number |

*Subscripts*

| | |
|---|---|
| aw | adiabatic wall temperature |
| p | particle (water drolet) |
| Pr | pressure gradient effects |
| s | solid |
| ∞ | bulk flow |

tempering using the method of air jet impingement heat transfer on large jet-to-plate distances. In this regard, we remark that very few studies have focused on glass tempering with the air/mist jet impingement and the heat transfer uniformity for the jet impingement heat transfer under conditions of small jet-to-plate distance and high temperature difference between the inlet and plate. Several empirical correlations were suggested for the air jet, while whose for the air/mist jet are still limited. This study aims to ensure ultra-thin glass tempering, which is helpful in investigating the effect of the mist parameters on the heat transfer rate and the uniformity of air/mist impinging jets under the condition of a small jet-to-plate distance. This study also propose the use of the surface standard deviation percentage of the Nusselt number as a quantitative estimator for the heat transfer uniformity. The surface-averaged temperature, averaged Nusselt number, surface-averaged Nusselt number, and surface standard deviation percentage of the Nusselt number obtained from the numerical studies are presented in an attempt to quantify the heat transfer rate and the uniformity. The current simulation is conducted at a fixed Reynolds number $Re = 30,000$, which is based on the hydraulic diameter of the circular jet [21], a fixed jet-to-plate spacing ($H/D = 0.2$) [38], the mist flow droplets diameters that varied from 5 to 20 μm, a nozzle inlet temperature that varied from 283 K to 303 K, and 5% and 10% mass fraction of the mist flow. These data will be useful in understanding the heat transfer rate and the uniformity of the mist flow jet impingement at a small jet-to-plate distance and in understanding that designing an air/mist jet impingement system has a certain theoretical importance.

## 2. Method

We use the Eulerian model (EM) and the discrete phase model (DPM) to simulate the continuous and discrete phase, respectively, in our two-phase flow scenario.

### 2.1. Governing equations of the continuous phase

The transient transport equations of mass, momentum, energy, and species are presented as follows [22]:

$$\frac{\partial \rho}{\partial t} + \frac{\partial}{\partial X_i}(\rho u_i) = S_m \tag{1}$$

$$\frac{\partial}{\partial t}(\rho u_j) + \frac{\partial}{\partial X_i}(\rho u_i u_j) = \rho g_j - \frac{\partial P}{\partial x_j} + \frac{\partial}{\partial x_i}\left(\tau_{ij} - \rho\overline{u_i'u_j'}\right) + F_j \tag{2}$$

$$\frac{\partial}{\partial t}(\rho C_p T) + \frac{\partial}{\partial X_i}(\rho C_p u_i T) = \frac{\partial}{\partial X_i}\left(\lambda\frac{\partial T}{\partial X_i} - \rho C_p\overline{u_i'T'}\right) + \mu\varnothing + S_h \tag{3}$$

$$\frac{\partial}{\partial t}(\rho C_j) + \frac{\partial}{\partial X_i}(\rho u_i C_j) = \frac{\partial}{\partial X_i}\left(\rho D_j\frac{\partial C_j}{\partial X_i} - \rho\overline{u_i'C_j'}\right) + S_j \tag{4}$$

where $\mu\varnothing$ is viscous dissipation; $\lambda$ is thermal conductivity; $C_j$ is the mass fraction of species j; $S_j$ is the source term for this species; $D_j$ is the diffusion coefficient of species j; $\rho\overline{u_i'u_j'}$, $\rho C_p\overline{u_i'T'}$ and $\rho\overline{u_i'C_j'}$ represent the Reynolds stresses, turbulent heat fluxes, and turbulent concentration (or mass) fluxes, respectively; $\tau_{ij}$ is the symmetric stress tensor [22]; and $S_m$, $F_j$, and $S_h$ represent the source terms of mass, momentum, and energy, respectively. These terms are calculated via the following equations [37]:

$$S_m = \frac{\Delta m_p}{m_{p,0}}\dot{m}_{p,0} \tag{5}$$

$$F_j = \sum\left(\frac{18\mu C_d R_e}{\rho_p d_p^2 24}(u_p - u) + F_{other}\right)\dot{m}_p\Delta T \tag{6}$$

$$S_h = \left[\frac{\overline{m}_p}{m_{p,0}}c_p\Delta T + \frac{\Delta m_p}{m_{p,0}}\left(-h_{fg} + \int_{T_{ref}}^{T_p}C_{p,i}dT\right)\right]\dot{m}_{p,0} \tag{7}$$

where $\dot{m}_p$ represents the mass flow rate of the droplets; $\Delta m_p$ is the total evaporated water mass in control volume; $\overline{m}_p$ is the average droplet mass in the control volume; and $m_{p,0}$ is the initial droplet mass at the inlet.

## 2.2. Governing equations of the discrete phase

The droplet trajectory can be formulated by integrating the force balance on a given particle, which can be written as follows using the Lagrangian approach [23]:

$$\frac{du_p}{dt} = F_D(u - u_p) + \frac{g_x(\rho - \rho_p)}{\rho_p} + F_x \tag{8}$$

where $F_x$ denotes the additional acceleration force, and $F_D(u - u_p)$ is the drag force per unit particle mass.

$$F_D = \frac{18\mu}{\rho_p d_p^2} \frac{C_D R_{e_d}}{24} \tag{9}$$

where $u$ denotes the fluid phase velocity; $u_p$ is the particle velocity; $\mu$ is the molecular viscosity of the fluid; $\rho$ is the fluid density; $\rho_p$ is the particle density; $d_p$ is the particle diameter, and $R_{e_d}$ is the relative Reynolds number defined as follows [23]:

$$R_{e_d} = \frac{\rho d_p |u_p - u|}{\mu} \tag{10}$$

The drag coefficient ($C_D$) for a smooth spherical droplet defined in Eq. (10) is a function of the Reynolds number [23]:

$$C_D = a_1 + \frac{a_2}{R_{e_d}} + \frac{a_3}{R_{e_d^2}} \tag{11}$$

where $a_1$, $a_2$, and $a_3$ are the constant parameters obtained from the experimental correlation [24].

As noted earlier, $F_x$ in Eq. (8), incorporates additional forces in the particle force balance, which can be important under special circumstances, such as those involving Virtual Mass Force and Pressure Gradient Effects.

$$F_x = F_v + F_{Pr} \tag{12}$$

where $F_v$ denotes the virtual mass force, and $F_{Pr}$ denotes the pressure gradient effects.

## 2.3. Droplet heat transfer

The rate of temperature change for the giving particle once the surface temperature reaches the saturation temperature of the droplets can be written as Eq. (13) upon considering the droplet as an isothermal system ($B_i < 0.1$).

$$\frac{d(m_p \cdot T_p \cdot C_w)}{dt} = \pi d_p k N_{u_p} (T_\infty - T_p) + \frac{dm_p}{dt} h_{fg} \tag{13}$$

where $c_w$ represents the specific heat of water; $T_p$ is the droplet temperature; $T_\infty$ is the continuous phase temperature; $dm_p/dt$ is the evaporation rate; and $h_{fg}$ is the latent heat of vaporization.

The convective heat transfer coefficient ($h$) can be obtained as follows using the empirical correlation derived by Ranz and Marshall [25,26]:

$$N_u = \frac{h d_p}{k_\infty} = 2 + 0.6 R_{e_d}^{0.5} P_r^{1/3} \text{ at } \quad 0 \leqslant R_{e_d} \leqslant 200 \tag{14}$$

where $d_p$ represents the droplet diameter; $k_\infty$ is the thermal conductivity of the continuous phase; $R_{e_d}$ is the Reynolds number; and $P_r$ is the Prandtl number of the continuous phase ($c_p \mu / k_\infty$).

## 2.4. Droplet mass transfer

The mass transfer rate is determined as follows, by the convective heat transfer when the droplet temperature reaches the boiling point:

$$\frac{d(m_p)}{dt} = -\pi d_p k N_{u_p} (T_\infty - T_p)/h_{fg} \tag{15}$$

The mass transfer rate when the droplet temperature is below the boiling point is given as follows:

$$\frac{d(m_p)}{dt} = \pi d_p \rho_v D_v Sh \left(\frac{M_v}{M}\right) log \left[\frac{1 - f_p}{1 - f}\right] \tag{16}$$

where $\rho_v$ and $D_v$ denote the density and diffusivity of vapor, respectively; Sh is the Sherwood number defined as the ratio of mass transfer by convection to mass transfer by diffusion; $M_v$ and $M$ are the molecular weights of the vapor and the mixture in the continuous phase, respectively; And $f_p$ and $f$ are the molar fractions in the droplet and the gas phase, respectively. Sh can be expressed as follows:

$$Sh = 2 + 0.6 R_{e_p}^{0.5} (P_r)^{0.3} \tag{17}$$

The stochastic method [27] is used to consider the turbulent dispersion effect on droplet tracking. The droplet trajectories are calculated using the instantaneous flow velocity $(\bar{u} + u')$. The velocity fluctuations are then provided as follows:

$$u' = \zeta (\overline{u'^2})^{0.5} = \zeta (2k/3)^{0.5} \tag{18}$$

where $\zeta$ represents a normally distributed random number.

## 3. Geometry

Fig. 1 shows the geometry of the computational domains, where the air and mist through a circular tube vertically impinging on a glass plate with 100 mm length, 70 mm width, and 2 mm thickness. The jet inlet shape was made circular, (diameter: 5 mm; length: 6 mm) to obtain a higher heat transfer efficiency. In the glass tempering process, the glass plate temperature varied with the cooling time. With the glass plate initial temperature set at 873 K, we consider the heat transfer characteristics using conjugate heat transfer between the fluid and solid domain. The top part of Fig. 1 was the fluid domain, while the bottom part was the solid domain with glass as the constituent material. The glass plate density was fixed at 2500 kg/m³, while the specific heat capacity and thermal conductivity varied with the temperature. Table 1 shows the thermal physical properties of glass.

The flow was assumed to be a three-dimensional, incompressible turbulent flow. The radiation heat transfer effects were neglected. A structural mesh was created for the whole domain using the O-blocking option with the ANSYS ICEM CFD 15.0 package to improve the quality of the grid for capturing the near-wall flow phenomenon. Fig. 2 shows the exemplary grid used in the circular nozzle with $H/D = 0.2$. Dense meshes were used near the target plate. The jet inlet mesh was also encrypted.

## 4. Boundary conditions

### 4.1. Continuous phase

Dry air was injected at different jet inlet temperatures with a uniform velocity at a constant Reynolds number ($R_e = \rho D u / \mu = 30,000$) ($\dot{m} = 2.2076 \, e^{-3}$) and a 5% flow turbulence intensity. The jet inlet temperature ranged from 283 to 303 K. The flow was assigned along the Z-direction (Fig. 1). The wall in the fluid domain was adiabatic and had no slip.

### 4.2. Discrete phase

The liquid droplets (mist) were treated as a discrete phase. The average droplet diameter varies between 5, 10, 15, and 20 μm at a
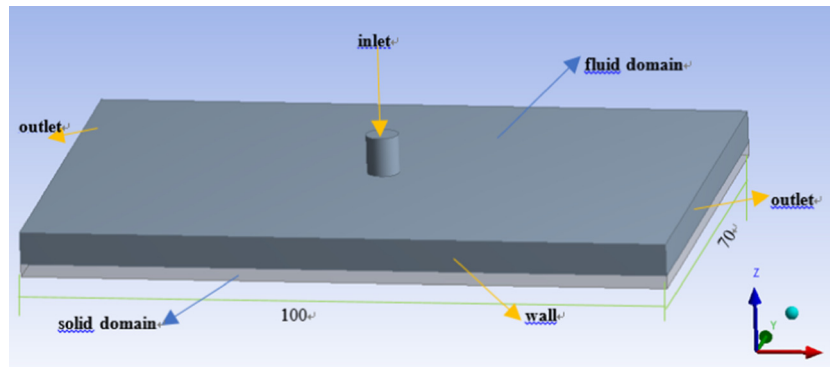
**Fig. 1.** Geometry of the computational domains.

**Table 1**
Thermal physical properties of glass.

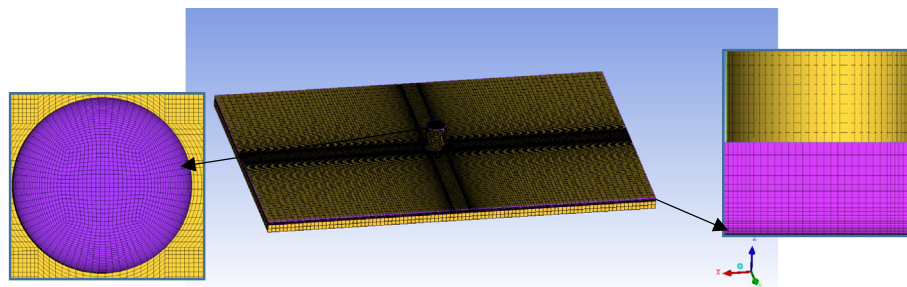| Temperature K | 298 | 373 | 473 | 573 | 673 | 773 | 873 |
|---|---|---|---|---|---|---|---|
| Specific heat J/(kg K) | 721 | 838 | 946 | 1036 | 1084 | 1108 | 1146 |
| Thermal conductivity W/(K m) | 1.4 | 1.47 | 1.55 | 1.67 | 1.84 | 2.04 | 2.46 |



**Fig. 2.** Mesh of the computational domain used for our study.

temperature of 300 K. The interaction between the continuous and discrete phases was considered. Unsteady tracking was used to track the particle. Moreover, the particle distribution was set to "uniform". The mass fraction of mist over airflow was 5% (approximately $1.1038 \times 10^4$ kg/s for mist), and 10% (approximately $2.2076 \times 10^{-4}$ kg/s for mist). The number of mist injection points at the velocity-inlet generally depended on the number of computational meshes at the inlet surface. One injection point was placed in each cell at the inlet surface. The total number of points was 2565. The boundary condition of the droplets at the pressure-outlet was assigned as "escape".

The droplets exhibited three major regimes along a dry wall: reflect, breakup, and trap. Watchers et al. [29] stated that the regimes depended on the Weber number of the incoming droplet. The Weber number is defined as the ratio of the kinetic energy of the droplet to its surface tension energy ($W_e = \rho d_p u_p^2 / \sigma$).

The boundary of droplets at the wall was assigned herein as "reflect" ($W_{e_{in}} = 10$), which meant that the droplets elastically rebounded after striking the wall [30].

## 5. Simulation

The numerical simulations were performed using the commercial computational fluid dynamics solver, Fluent 15.0. The flow, turbulence, energy, and species equations were solved. The SIMPLEC algorithm was applied to the pressure velocity coupling. Meanwhile, the second-order upwind discretization scheme was

used for the pressure, momentum, turbulent kinetic energy, specific dissipation rate, species, and energy. The realizable k–ε turbulent model with an enhanced wall treatment was included in the simulation to obtain more accurate results for describing the jet dynamics.

Herein, we first validated the grid independence. We then compared the effect of mist flow jet impingement on heat transfer under different conditions through the surface-averaged temperature, averaged-Nusselt number, and surface-averaged Nusselt number. Finally, the surface standard deviation percentage of the Nusselt number was used in an attempt to quantify the heat transfer uniformity in the mist flow jet impingement process on a glass plate.

## 6. Results and discussion

### 6.1. Grid independence analysis

Air was treated as a fluid medium in our analysis. Fig. 3 shows the results of grid independence analysis. A careful grid independence check was conducted by considering several grid system, with nodes ranging from 498,549 to 1,167,749. The nodes ranging from 498,549 to 1,167,749 corresponding to the $H$ of 2 mm were used as 15- to 40-layer nodes, respectively. A comparison of the numerical results (Fig. 3) with the experimental results [7] showed that the difference in the simulation results between the 498,549 to 1,167,749 cases was less than 1%. Therefore, a grid density of 900,069 nodes was used in our simulations.
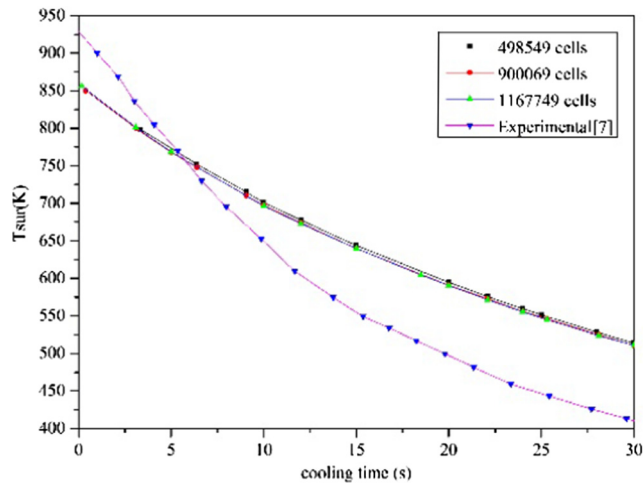
**Fig. 3.** Grid independence at $R_e = 30,000$.



**Fig. 4.** Stagnation point Nusselt number as a function of *Re* number, as obtained in various studies.

The local Nusselt number can be expressed as follows [31,32]:

$$N_u(x,y) = \frac{h(x,y)D}{k} = \frac{q''D}{[T_w(x,y) - T_{aw}(x,y)]k} \tag{19}$$

where $T_w$ is the wall temperature; $T_{aw}$ is the adiabatic wall temperature; $D$ is the hydraulic diameter of the circular jet; $k$ is the thermal conductivity for the continuous phase; $h$ is the heat transfer coefficient; and $q''$ is the wall heat flux.

The averaged Nusselt number can be expressed as follows [31,32]:

$$N_{u_{ave}} = \int_{x=x_0}^{y=y_i} \frac{1}{\Delta y} N_u(x,y) dy \tag{20}$$

The surface averaged Nusselt number can be expressed as:

$$\overline{N_u} = \frac{1}{A} \int \phi N_u(x,y) dA = \frac{1}{A} \sum_{i=1}^{n} \Phi_i N_u(x,y)|A_i| \tag{21}$$

Meanwhile, the surface standard deviation percentage of the Nusselt number can be expressed as follows [33]:

$$\sigma_{N_u(x,y)} = \frac{\sqrt{\int_{x=x_0}^{y=y_i} \frac{1}{\Delta y} (N_u(x,y) - N_{u_{ave}})^2 dy}}{N_{u_{ave}}} \tag{22}$$

### 6.2. Numerical method validation

Bian et al. [20] concluded that the realizable k–ε provided satisfactory results for modeling the mist jet impingement heat transfer by conjugate heat transfer. Torfeh and Kouhikamali [17] also found that the realizable k–ε obtained better results by comparing the error of the numerical heat transfer coefficient with the empirical correlation. In [34], the realizable k–ε turbulence model was used to more accurately describe the jet dynamics in the calculations. We simulated the stagnation point Nusselt number for different *Re* using the realizable k–ε turbulence model to make a comparison with the available experimental correlation ($N_{u_0} = 0.663R_e^{0.53}(H/D)^{-0.248}$) corresponds to the experimental data obtained for a small jet-to-plate distance (Fig. 4). Fig. 4 shows that the trends of the realizable model and the experimental data were similar, and the maximum relative error of 14%. The reason for this difference mainly originated from the variation in the jet diameter and the geometry size. The radiation heat transfer was neglected in our simulations, but its effect still existed in the work of [28]. The thermal boundary condition of the impingement
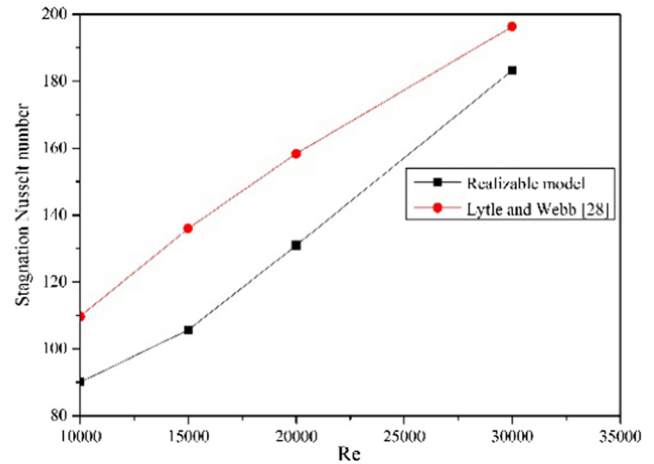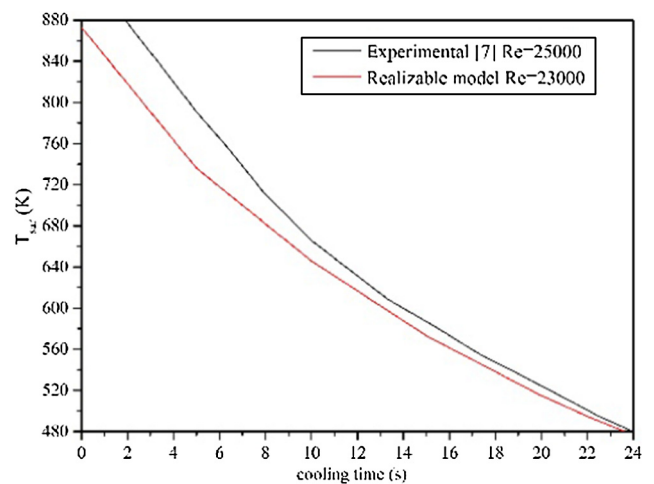


**Fig. 5.** Temperature variation as a function of cooling time.
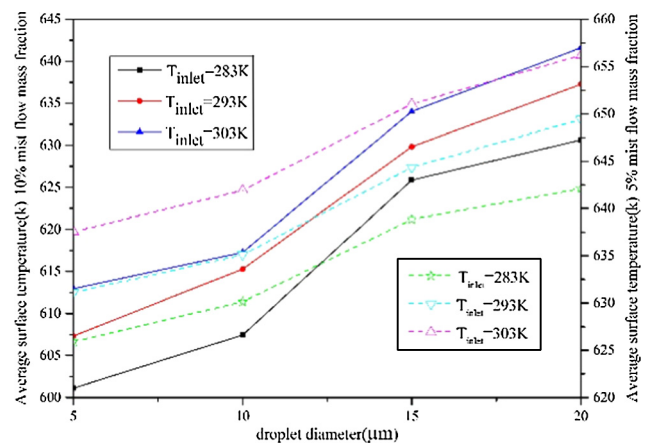


**Fig. 6.** The dependence of average surface temperature on droplet diameters for different jet inlet temperature.

surface was also an important factor. Zhu et al. [35] concluded that the conjugate effect led to a decay of the Nusselt number, which meant that the results of the numerical predictions obtained with the conjugate heat transfer are underestimated.
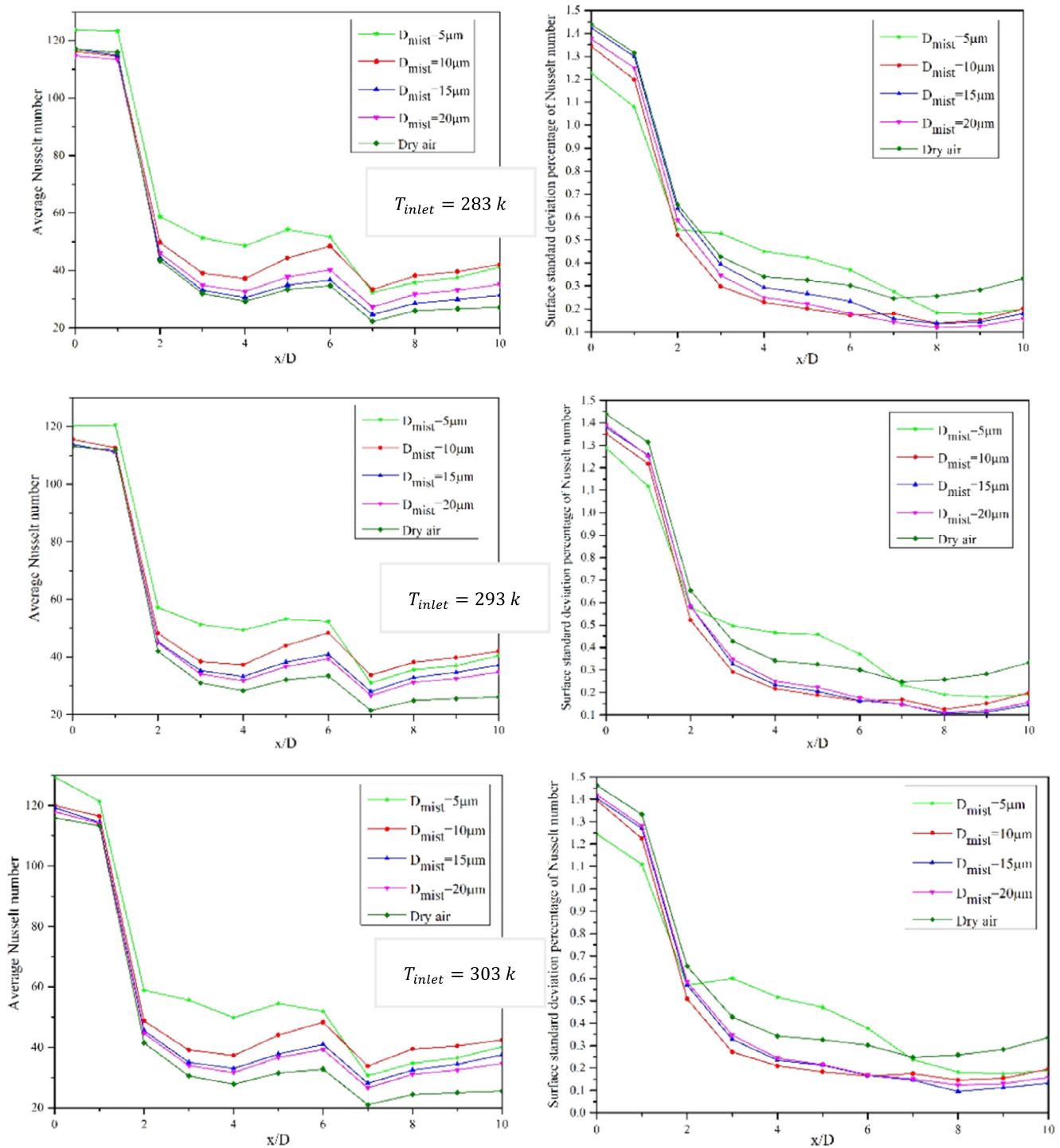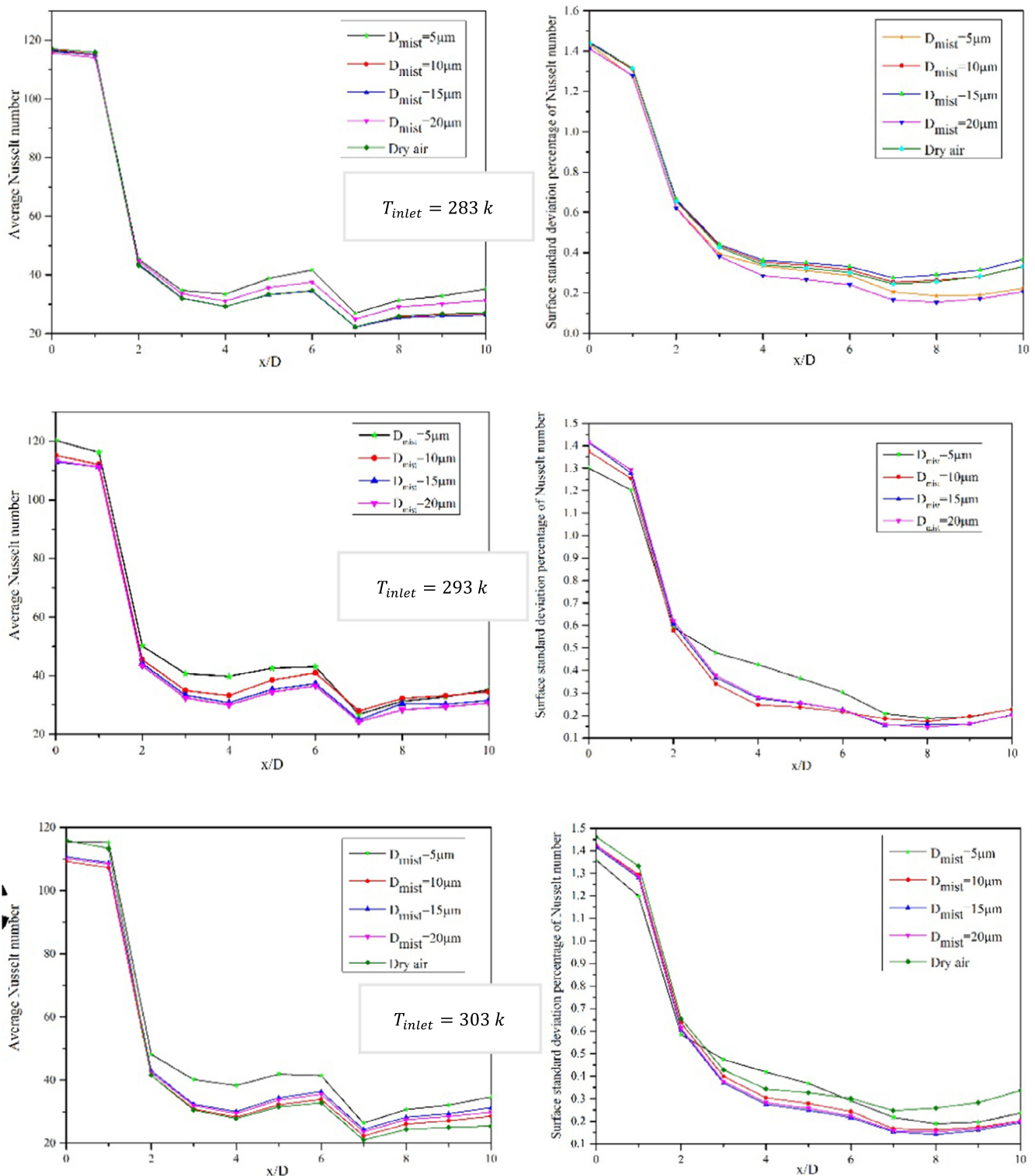
**Fig. 7.** Distributions of $N_{u_{ave}}$ and $\sigma_{N_u}$ in the downstream direction for different jet inlet temperature (10% mist flow mass fraction).

The surface temperature variation as a function of cooling time was simulated with the realizable k–ε to further verify the accuracy of the numerical method and make a comparison with the experimental results (Fig. 5) [7]. The results obtained by Yazici et al. [7] corresponded to the experimental data obtained for the transient temperature distribution and the heat transfer by jet impingement in the glass tempering process. Fig. 5 presents a maximum relative error of 5%, which was comparable to that obtained by Yazici et al. [7]. The comparison of the results revealed that the present numerical method was reasonable and acceptable.

### 6.3. Effects of the mist flow droplet diameter on the heat transfer rate and uniformity

Fig. 6 illustrates the dependence of the average surface temperature on different droplet diameters for different jet inlet temperature and mist flow mass fraction. As shown in Fig. 6, the lowest average surface temperature for all cases was 600 K. Garcimoreno [36] visually determined that for the tested drop size distribution, the water droplets do not impinge on the plate surface at a plate temperature above 473 K. The most probable droplet diameter in

**Fig. 8.** Distributions of $N_{u_{ave}}$ and $\sigma_{N_u}$ in the downstream direction for different jet inlet temperature (5% mist flow mass fraction).

his experiments was 18 μm. The droplet diameters used in our study were lower than this value. Therefore, we can assume that vaporization has occurred before the water droplets reached the high-temperature glass plate surface, and the enhancement of heat transfer on the glass plate wass mainly attributed to the latent heat of the droplet evaporation. We ignored the heat transfer arising from drop-wall impact.

Fig. 6 further shows that for the same jet inlet temperature, the larger the droplet diameter, the higher the average surface temper-

ature. Moreover, the surface temperature first slowly increased with the increase of the droplet diameter, then abruptly increased with the droplet diameters of 10–15 μm, and finally slowly increased with further increases in the droplet diameter. This behavior was mainly caused by the increased number of droplets ejected from the inlet as the droplet diameter decreases. Thus, an increased number of droplets evaporated, resulting in a faster surface temperature reduction caused by the latent heat of droplet vaporization. In addition, the heat and the time required for com-

plete vaporization of the droplets increased with the increase of droplet diameter.

The average surface temperature clearly increased as the mist flow mass fraction decreased for all of the case. The differences of the average surface temperature between the different droplet diameters became lesser at the same jet inlet temperature when the mist flow mass fraction decreased.

Therefore, the droplet diameter should be kept at 5–10 μm which allowed for a higher heat transfer efficiency and enhanced heat transfer, to obtain thinner tempered glass.

A comparison between the mist flow with different droplet diameters and dry air on the distributions of $N_{u_{ave}}$ and $\sigma_{N_u}$ is shown in Fig. 7 for different jet inlet temperature, with a mist flow mass fraction of 10%, to verify the effects of the droplet diameters on heat transfer.

The left side presents the distribution of $N_{u_{ave}}$ along the downstream direction, while the right shows the distribution of $\sigma_{N_u}$ along the downstream direction. Fig. 7 also shows that $N_{u_{ave}}$ first slowly decreased, then drastically decreased. The curves also overlapped. A second peak occurred at the wall jet region with the increase of the downstream direction. The peak position shifted downstream as the droplet diameters increased. Moreover, a second peak existed downstream at $x/D = 6$. The main reason for this phenomenon is the higher heat transfer efficiency at the stagnation region, resulting to the highest $N_{u_{ave}}$ in the $x/D \leqslant 1$ region. The formation of this second peak was attributed to the small jet-to-plate distance and to the laminar-to-turbulent boundary transition in the wall jet region.

Comparing the dry air and the mist flow, $N_{u_{ave}}$ increased with the decrease of droplet diameter. Furthermore, the dry air obtained the lowest $N_{u_{ave}}$ value. The $N_{u_{ave}}$ variation between the dry air and the mist flow was not obvious when $x/D \leqslant 2$. However, the difference gradually increased with the downstream increase. This phenomenon was caused by the relatively large kinetic energy of air at the stagnation region and the heat removed from the latent heat of evaporation being not particularly obvious. In addition, the mainstream temperature increased downstream in the downstream direction, causing a reduction of the heat transfer efficiency. The kinetic energy of the air also decreases as the main flow moved along the stagnation region toward the wall jet region, leading to a decrease in $N_{u_{ave}}$. Compared with the dry air, the latent heat of the droplet vaporization of the jet impingement heat transfer removed part of the heat. Moreover, the stream generated by the droplet vaporization increased the specific heat capacity and the kinetic energy of the mainstream, causing an enhanced convection heat transfer capacity. During the flow towards the wall jet, the latent heat of droplets carried by the mainstream makes up the effect of the decrease of the kinetic energy of the mainstream on the heat transfer rate, which justified why $N_{u_{ave}}$ of the dry air was lower than that of the downstream mist flow along the downstream direction.

The right side demonstrated that $N_{u_{ave}}$ and $\sigma_{N_u}$ had similar trends. As $N_{u_{ave}}$ becomes higher, $\sigma_{N_u}$ becomes higher, which reveals that this position has s high heat transfer rate and poor heat transfer uniformity. In the comparison of dry air and mist flow, excluding the $D_{mist} = 5$ μm case, the cases show a similar trend in which the distribution of $\sigma_{N_u}$ shows a decreasing trend along the downstream direction. Moreover, when $x/D = 6 - 7$, there exists a turning point, corresponding to the trend of $N_{u_{ave}}$ at the similar position, which is mainly due to the effect of the secondary peak at the downstream.

Further comparing the effects of the dry air and mist flow on $N_{u_{ave}}$ and $\sigma_{N_u}$, we can conclude that the mist flow had a higher heat transfer rate and a better heat transfer uniformity than the dry air. The smaller the droplet diameters, the higher the heat transfer

rate. However, note that the heat transfer uniformity was not higher. The heat transfer uniformity was better at the stagnation point region of $D_{mist} = 5$ μm, and was the best at the wall jet region of $D_{mist} = 10$–15 μm.

Fig. 8 depicts a comparison of the mist flow with different droplet diameters and the dry air in terms of the $N_{u_{ave}}$ and $\sigma_{N_u}$ distributions for different jet inlet temperatures with a mist flow mass fraction of 5%.

The tendency of the $N_{u_{ave}}$ and $\sigma_{N_u}$ distribution was similar to the different mist flow mass fraction. $N_{u_{ave}}$ decreased with the decrease of the mist flow mass fraction. Moreover, the heat transfer uniformity of the mist flow with different mass fractions was always higher than that of the dry air. However, $\sigma_{N_u}$ was independence of the mist flow mass fraction. Therefore, we can conclude that the heat transfer rate increased with the increase of the mist flow mass fraction, and the heat transfer uniformity was almost the same.

Fig. 9 presents the dependence of $\overline{N_u}$ on the droplet diameter for different jet inlet temperature. $\overline{N_u}$ decreased, then increased as the droplet diameter increased. The turning point occurred at $D_{mist} = 18$ μm. The results corresponded to the data in Fig. 6, in
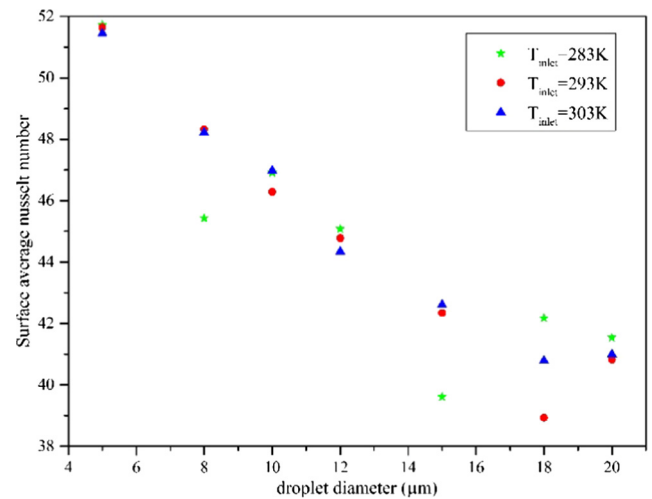


**Fig. 9.** The dependence of $\overline{N_u}$ on droplet diameter for different jet inlet temperature.
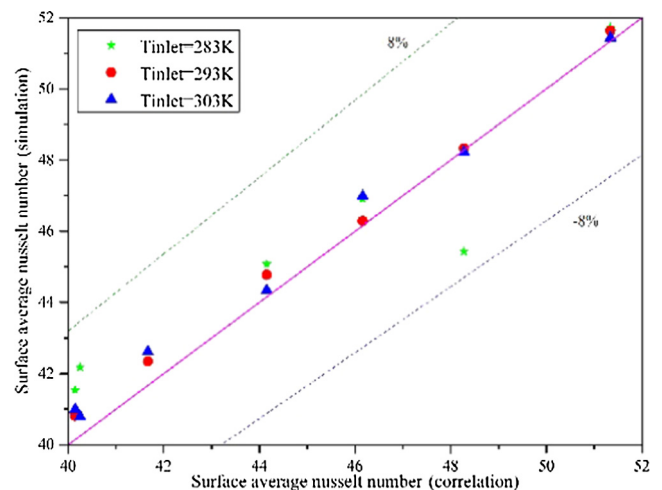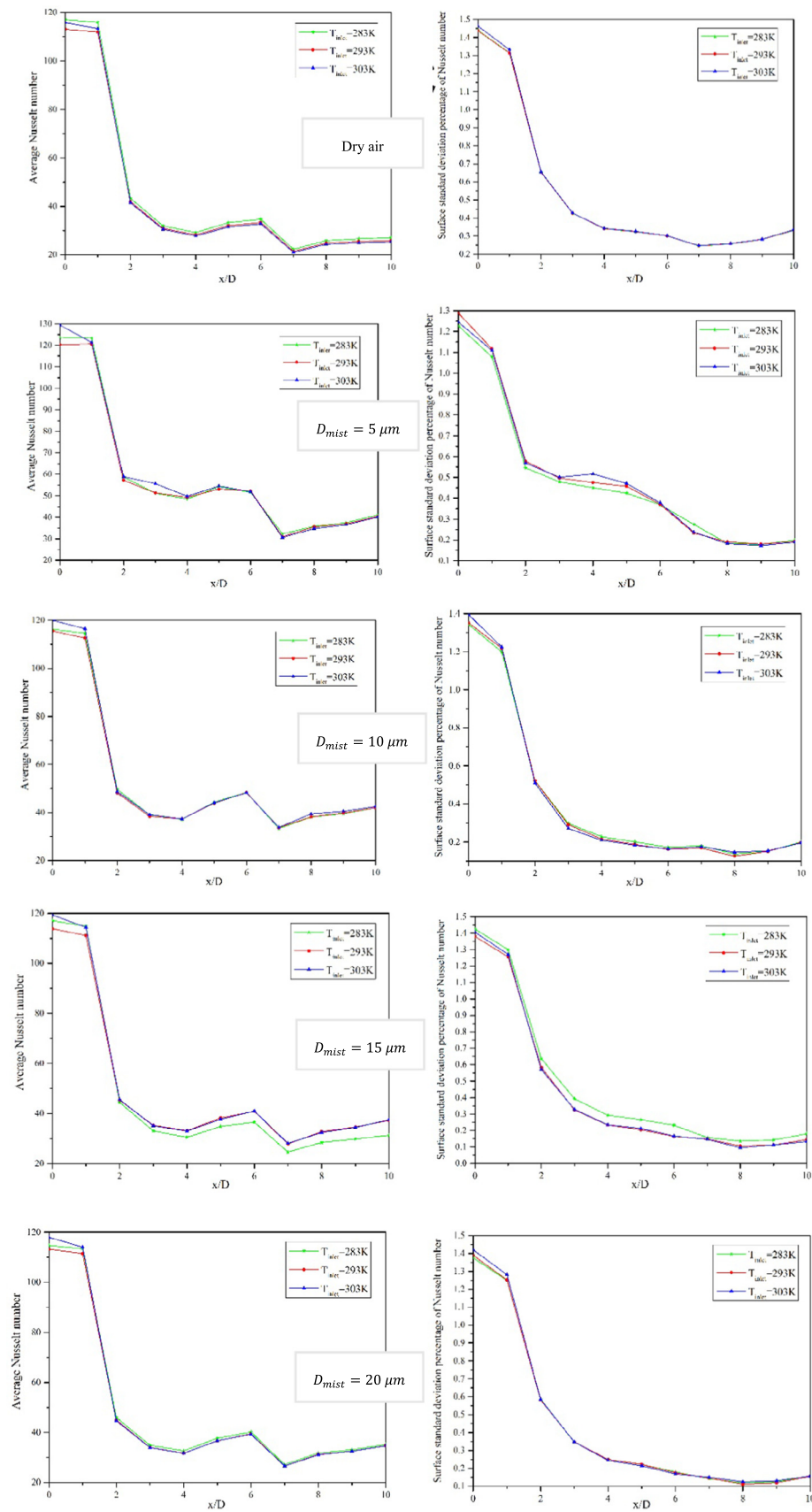


**Fig. 10.** Comparison of simulations and correlations.

**Fig. 11.** Distributions of $N_{u_{ave}}$ and $\sigma_{N_u}$ in the downstream direction for different droplet diameter (10% mist flow mass fraction).

which the average surface temperature decreased as $\overline{N_u}$ increased. The empirical correlation for $\overline{N_u}$ as a function of mist flow droplet diameters can be expressed as follows:

$$\overline{N_u} = 54.94954 - 0.41197D_m - 0.07701D_m^2 + 0.00313D_m^3 \qquad (23)$$

The $\overline{N_u}$ correlation results were then compared with those of the numerical simulations. The correlation results were within ±8% of the numerical results (Fig. 10).

### 6.4. Effects of different jet inlet temperatures on the heat transfer rate and uniformity

Fig. 11 shows the $N_{u_{ave}}$ and $\sigma_{N_u}$ distributions for different droplet diameter. The distribution curves of $N_{u_{ave}}$ exhibited a similar tendency along the downstream direction for different droplet diameters, and a peak existed at $x/D = 6$, as described in the cases shown in Figs. 7 and 8.

An obvious difference also existed in $N_{u_{ave}}$ at $x/D \leqslant 1$. Furthermore, the $N_{u_{ave}}$ curves overlapped in the downstream direction of $x/D \geqslant 1$ for all the cases. The main reason for these results are the higher $P_r$ when the jet inlet temperature was lower and the stronger heat transfer at the stagnation point region. The kinetic energy of the fluid gradually decreased downstream after the stagnation point region. Moreover, the fluid temperature increased with the increase in the cooling time. The temperature difference between the inlet and the plate surface also decreased. Finally,

the effect of the surface heat transfer approached the same trend. Thus, $N_{u_{ave}}$ had a significant difference at the stagnation point region along the downstream direction.

More heat could be removed from the fluid as the jet inlet temperature became lower. In addition, the surface temperature of the glass plate decreased. The droplet temperature was 300 K when the jet inlet temperature was very low, such that the evaporated vapor was easy to condense and resulted in the deteriorates the local surface average heat transfer. This trend was observed in Fig. 9, where the jet inlet temperature decreased, but $\overline{N_u}$ did not increase. Therefore, jet inlet temperature and the droplet diameter must be well matched if we want to obtain the best heat transfer rate.

Fig. 11 shows that the lower the jet inlet temperature, the smaller the $\sigma_{N_u}$ of $x/D \leqslant 1$. The jet inlet temperature has a little effect on $\sigma_{N_u}$ of $x/D \geqslant 1$.

Hence, we can conclude that $\sigma_{N_u}$ decreased with the decrease of the jet inlet temperature. In other words, the heat transfer uniformity was better even though the local heat transfer rate was not higher.

### 6.5. Temperature distribution

Fig. 12 illustrates the contours of surface temperature with the mist flow mass fraction of 10% and jet inlet temperature of 283 K for different droplet diameters. The figure shows that the temperature at the stagnation point region was the lowest, but was the
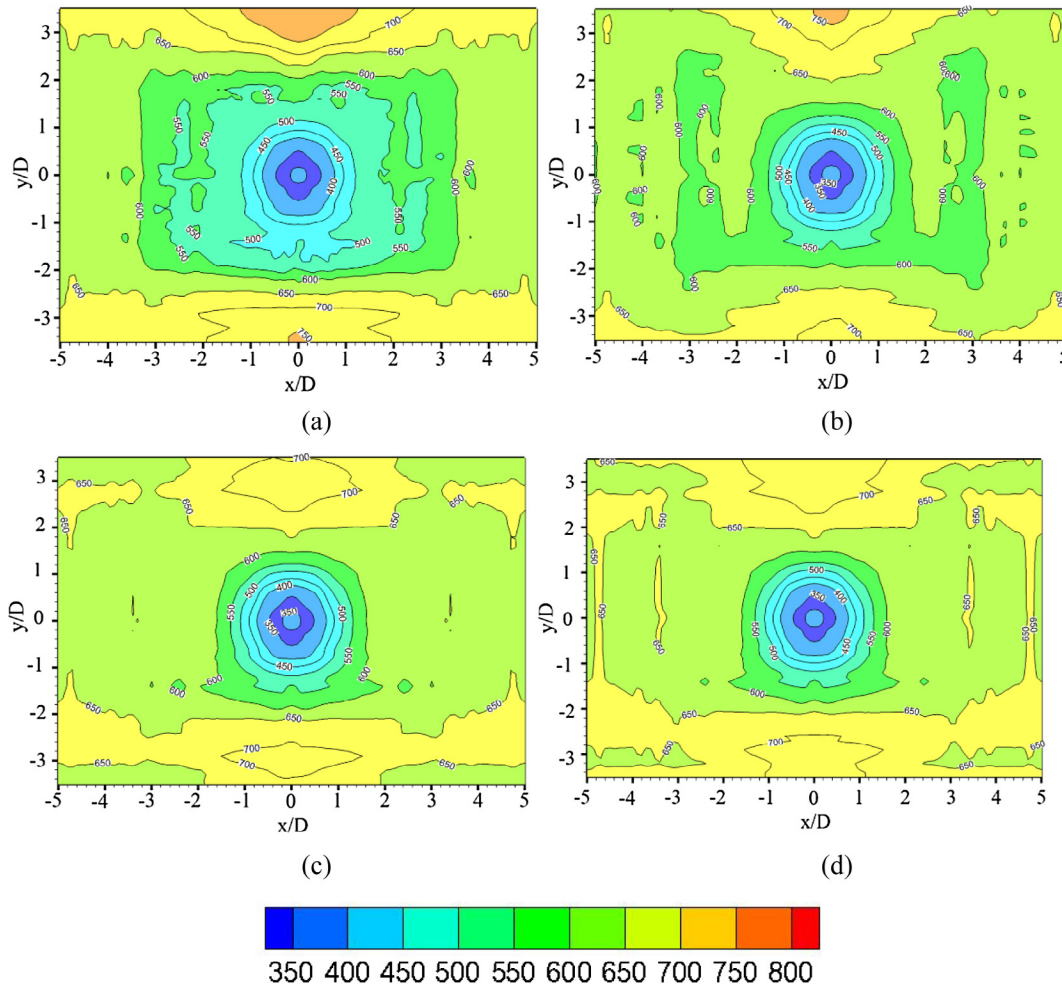


**Fig. 12.** Surface temperature contour (K), (a) $D_{mist} = 5\,\mu m$, (b) $D_{mist} = 10\,\mu m$, (c) $D_{mist} = 15\,\mu m$, (d) $D_{mist} = 20\,\mu m$.

same for different droplet diameters. Meanwhile, the temperature besides the stagnation point region increased, especially at the wall jet region. The average surface temperature increased with the increase of the droplet diameter.

## 7. Conclusions

In this study, the characteristics of the heat transfer rate and heat transfer uniformity under the conditions of a small jet-to-plate distance and a high temperature difference between the nozzle inlet and the glass plate were numerically obtained.

In conclusion, the larger the droplet diameter, the higher the average surface temperature. The difference of the average surface temperature between the different droplet diameters became less with the decrease of mist flow mass fraction. Hence, the droplet diameter must be kept at 5–10 μm to obtain thinner tempered glass.

The $N_{u_{ave}}$ first slowly decreased, then drastically decreased. A second peak value of the $N_{u_{ave}}$ was also observed downstream of the flow. Comparing the effects of the dry air and mist flow on $N_{u_{ave}}$ and $\sigma_{N_u}$, we note that the smaller the droplet diameters, the higher the heat transfer rates. However, the heat transfer uniformity was not improved. The heat transfer uniformity was better at the stagnation point region of $D_{mist} = 5$ μm, and was the best at the wall jet region of $D_{mist} = 10$–15 μm.

The empirical correlation for $\overline{N_u}$ as a function of mist flow droplet diameters was provided at different jet inlet temperatures. We note that the heat transfer uniformity increased with the decrease of the jet inlet temperature, while the heat transfer rate increased and subsequently decreased.

Using the mist flow jet impingement, we would not only greatly reduce the amount of air and save energy, but also meet the needs of sudden cooling for tempered glass with a thickness of less than 2 mm, by optimizing the mist flow parameters and the jet impingement structure.

## Acknowledgements

## Conflict of interest

The authors declared that there is no conflict of interest.

## References

[1] S. Türkbas, Ö.E. Ataer, Numerical modelling of heating and cooling processes in glass tempering with mixed boundary conditions, J. Fac. Eng. Arch. Gazi Univ. 22 (2007) 727–738.

[2] F. Monnoyer, D. Lochegnies, Heat transfer and flow characteristics of the cooling system of an industrial glass tempering unit, Appl. Therm. Eng. 28 (2008) 2167–2177.

[3] M. Golcu, H. Yazici, M. Akcay, M.F. Koseoglu, Y. Sekmen, Experimental investigation of cooling with multiple air jets on auto glass tempering, J. Fac. Eng. Arch. Gazi Univ. 27 (2012) 775–783.

[4] J.Y. San, M.D. Lai, Optimum jet-to-jet spacing of heat transfer for staggered arrays of impinging air jets, Int. J. Heat Mass Transf. 44 (2001) 3997–4007.

[5] H. Yazici, Determination of Optimum Cooling Unit Configuration in Automobile Glass Tempering Process by Different Reynolds Number, PhD Thesis, Karabuk University, Turkey.

[6] H. Yazici, M. Akcay, M. Golcu, M.F. Koseoglu, Y. Sekmen, Experimental investigation of the transient cooling characteristics of an Industrial Glass tempering unit, World Acad. Sci. Eng. Technol. 61 (2012) 207–211.

[7] H. Yazici, M. Akcay, M. Golcu, M.F. Koseoglu, Y. Sekmen, Experimental investigation of the transient temperature distribution and heat transfer by jet impingement in glass tempering processing, IJST. Trans. Mech. Eng. 39 (2016) 337–349.

[8] B.W. Fan, K.Q. Zhu, Q. Shi, T. Sun, N.Y. Yuan, J.N. Ding, Effect of glass thickness on temperature gradient and stress distribution during glass tempering, J. Non-Cryst. Solids 437 (2016) 72–79.

[9] H. Ohkubo, S. Nishio, Mist Cooling for Thermal Tempering of Glass, Jpn. Soc. Mech. Eng. Int. J. Ser. II 31 (1988) 444–450.

[10] N. Sozbir, S.C. Yao, Experimental investigation of water mist of water mist cooling for glass temperature, Atomization Sprays 14 (2004) 191–210.

[11] N. Sozbir, S.C. Yao, Spray mist cooling heat transfer in glass tempering process, Heat Mass Transf. (2016) 1–13.

[12] W.L. Cheng, Q.N. Liu, R. Zhao, H.L. Fan, Experimental investigation of parameters effect on heat transfer of spray cooling, Heat Mass Transf. 46 (2010) 911–921.

[13] J. Ting Wang, Leo Gaddis, Xianchang Li, Mist/steam heat transfer of multiple rows of impinging jets, Int. J. Heat Mass Transf. 48 (2005) 5179–5191.

[14] Tan XiaoMing, Zhang JingZhou, Liu Bo, Zh.u. XingDan, Experimental investigation on heat transfer enhancement of mist/air impingement jet, Technol. Sci. 56 (2013) 2456–2464.

[15] C. Quinn, D.B. Murray, T. Persoons, Heat transfer behaviour of a dilute impinging air-water mist jet at low wall temperatures, Int. J. Heat Mass Transf. 111 (2017) 1234–1249.

[16] T.S. Dhanasekaran, Ting Wang, Computational analysis of mist/air cooling in a two-pass rectangular ratating channel with 45-deg angles rib turbulators, Int. J. Heat Mass Transf. 61 (2013) 554–564.

[17] S. Torfeh, R. Kouhikamali, Numerical investigation of mist flow regime in a vertical tube, Int. J. Thermal Sci. 95 (2015) 1–8.

[18] Terekhov Pakhomov, The effect of confinement on the flow and turbulent heat transfer in a mist impinging jet, Int. J. Heat Mass Transf. 54 (2011) 4266–4274.

[19] M.A. Pakhomov, V.I. Terekhov, Enhancement of an impingement heat transfer between turbulent mist jet and flat surface, Int. J. Heat Mass Transf. 53 (2010) 3156–3165.

[20] Q. Bian, W. Jin, Y.T. Chen, Q. Wang, M. Zeng, Numerical investigation of mist/air impingement cooling on ribbed blade leading-edge surface, J. Environ. Manage. (2017).

[21] H. Yazici, M. Akcay, M. Golcu, M.F. Koseoglu, Y. Sekmen, Installation of auto glass experimental unit and a case study for determination of heating-cooling periods, Electron. J. Mach. Tech 8 (2011) 57–68.

[22] T.S. Dhanasekaran, T. Wang, Numerical model validation and prediction of mist/steam cooling in a 180-degree bend tube, Int. J. Heat Mass Transf. 55 (2012) 3818–3828.

[23] R. Kouhikamali, H. Hesami, A. Ghavamian, Convective heat transfer in a mixture of cooling water and superheated steam, Int. J. Therm. Sci. 60 (2012) 205–211.

[24] S.A. Morsi, A.J. Alexander, An investigation of particle trajectories in two-phase flow system, J. Fliud Mech. 55 (1972) 45–57.

[25] W.E. Ranz, W.R. Marshall Jr, Evaporation from drops, Part I. Chem. Eng. Prof. 48 (1952) 141–146.

[26] W.E. Ranz, W.R. Marshall Jr, Evaporation from drops, Part I. Chem. Eng. Prof. 48 (1952) 173–180.

[27] Ansys/Fluent manual, Ansys, Inc., 2010.

[28] D. Lytle, B.W. Webb, Air jet impingement heat transfer at low nozzle-plate spacing, Int. J. Heat Mass Transf. 37 (1994) 1687–1697.

[29] L.H.J. Wachters, L. Smulders, J.R. Vermeulen, H.C. Kleiweg, The heat transfer from a hot wall to impinging mist droplets in the spheroidal state, Chem. Eng. Sci. 21 (1996) 1231–1238.

[30] T.S. Dhanasekaran, T. Wang, Validation of mist/steam cooling CFD model in a horizontal tube, ASME 2008 Heat Transfer Summer Conference Collocated with the Fluids Engineering, Energy Sustainability and Energy Nanotechnology Conference, 2008, pp. 10–14.

[31] N.M. Elwekeel, M.M. Abdala, Effects of mist and jet cross-section on heat transfer for a confined air jet impinging on a flat plate, Int. J. Therm. Sci. 108 (2016) 174–184.

[32] F.P. Incropera, Fundamentals of Heat and Mass Transfer, John Wiley, Hoboken, NJ, 2007, p. 450.

[33] A. Ianiro, G. Cardone, Heat transfer rate and uniformity in multichannel swirling impinging jets, Appl. Therm. Eng. 49 (2012) 89–98.

[34] M. Garbero, M. Vanni, U. Fritsching, Gas/surface heat transfer in spray deposition processes, Int. J. Heat Fluid Flow 27 (2006) 105–122.

[35] X.W. Zhu, L. Zhu, J.Q. Zhao, An in-depth analysis of conjugate heat transfer process of impingement jet, Int. J. Heat Mass Transf. 104 (2017) 1259–1267.

[36] C.J. Garciamoreno, D.A. Everest, A. Arvind, Heat transfer in glass quenching for glass tempering, Ceram. Eng. Sci. Proc. 36 (2015) 235–252.

[37] N. Kumari, V. Bahadur, M. Hodes, T. Salamon, P. Kolodner, A. Lyons, S.V. Garimella, Analysis of evaporating mist flow for enhanced convective heat transfer, Int. J. Heat Mass Transf. 53 (2010) 3346–3356.

[38] P.P. Yu, K.Q. Zhu, Q. Shi, N.Y. Yuan, J.N. Ding, Transient heat transfer characteristics of small jet impingement on high-temperature flat plate, Int. J. Heat Mass Transf. 114 (2017) 981–991.